LIMNOLOGY
and
OCEANOGRAPHY

ASLO

Limnol. Oceanogr. 60, 2015, 2222–2235

doi: 10.1002/lno.10163

Shear dispersion from near-inertial internal Poincaré waves in large lakes

Jun M. Choi,[1] Cary D. Troy,*[1] Nathan Hawley[2]
[1]Lyles School of Civil Engineering, Purdue University, West Lafayette, Indiana
[2]NOAA Great Lakes Environmental Research Laboratory (GLERL), Ann Arbor, Michigan

Abstract

In this work, we study mixed layer lateral dispersion that is enhanced by near-inertial internal Poincaré waves in the offshore region of a large stratified lake, Lake Michigan. We examine the hypothesis that the vertical shear created by near-inertial internal Poincaré waves is not only an energy source for vertical mixing in the thermocline and mixed layer, but also enhances horizontal dispersion via an unsteady shear flow dispersion mechanism. Complex empirical orthogonal function analysis reveals that the dominant shear structure is observed to mirror the thermal structure, with the location of maximum shear gradually lowered as the mixed layer deepens. This changing structure of shear and vertical mixing produces different characteristics in shear flow dispersion between the early and later stratified periods. The estimated depth-averaged surface layer vertical turbulent diffusivity grows from 10^{-5} m^2s^{-1} to 10^{-3} m^2s^{-1} over the stratified period, and the associated lateral dispersion coefficients are estimated as 0.1–40 m^2s^{-1}. The Poincaré waves are found to enhance greatly lateral dispersion for times less than the inertial period following release. In contrast, subinertial shear is the dominant mechanism responsible for shear dispersion for times greater than the inertial period. A simple approximation of the dispersion coefficient for lateral dispersion is developed, which scales as the product of surface current velocity (or wind friction velocity) and mixed layer depth. The calculated dispersion coefficients agree well with Okubo's diffusion diagram for times up to a week, which suggests that unsteady shear dispersion is a plausible mechanism to explain observed dispersion rates in the mixed layer for early times after release.

The lateral spread of substances in the mixed layers of oceans and large lakes is directly driven by physical processes, and the development of relationships between particular physical processes and the net dispersion of natural and anthropogenic materials is an important step in the refinement of numerical models that can predict dispersion characteristics of algae (Wynne et al. 2011), larvae (Beletsky et al. 2007; North et al. 2008) and oil spills (Dietrich et al. 2012) in these systems. The focus of this article is the horizontal dispersion of substances released into the surface layer in an offshore region of a large stratified lake (Lake Michigan) and the role of near-inertial internal Poincaré waves—which dominate offshore surface lake currents for most of the year—on lateral dispersion. The results described herein should be expected to apply to other wind-driven ocean and lake systems where low-mode, near-inertial internal wave shear is dominant and persistent in the thermocline and mixed layer.

*Correspondence: troy@purdue.edu

Previous oceanic and large lake work has examined the roles of low-mode near-inertial internal wave shear in vertical mixing (MacKinnon and Gregg 2005; Van der Lee and Umlauf 2011; Bouffard et al. 2012), showing that these waves can cause substantial shear over pycnoclines, enhancing vertical mixing. However, while the role of internal wave-induced shear on lateral dispersion has been shown to be important (Steinbuck et al. 2011), to our knowledge no study has examined the role of low-mode near-inertial internal wave shear in surface layer lateral dispersion. In this article, a Lagrangian particle tracking model is used with ADCP-measured velocity fields to quantify lateral mixed layer dispersion and link it to physical processes.

Measurements have shown that near-inertial internal Poincaré waves dominate offshore surface currents in large lakes during the stratified period (Mortimer 2004; Bouffard et al. 2012; Choi et al. 2012; Austin 2013). At the center of southern Lake Michigan, for example, the internal Poincaré wave is frequently observed to account for more than 80% of the total kinetic energy of surface layer currents during the stratified period (Choi et al. 2012 and results described

herein). Internal Poincaré waves in Lake Michigan have a very low Burger number ($S_i \equiv \frac{c_i}{fR} \sim 10^{-2}$, where c_i is the long internal wave speed, f is the Coriolis parameter, and R is the basin radius; Antenucci and Imberger 2001), and thus the dominant Poincaré modes have near-inertial periods (17–18 h, typically). This near-inertial energy is manifested as clockwise-rotating (in the northern hemisphere) velocity fields that are largely in phase across the entire lake (Mortimer 2004; Ahmed et al. 2013); we show later that the vertical structure of the wave-induced currents is well-described by the lowest baroclinic (normal) mode.

With the large amount of offshore surface mixed layer energy associated with the internal Poincaré mode, a logical question is: how/do these waves affect lateral dispersion? One possible mechanism of dispersion enhancement from internal Poincaré waves is via a shear flow dispersion mechanism associated with the horizontal and/or vertical shear associated with the fundamental wave structure. In the horizontal direction, wave-induced current fields have a shear length scale of half the basin size, with maximum currents at the center of the basin decaying to negligible induced currents near shore (Antenucci and Imberger 2001; Ahmed et al. 2013). Stocker and Imberger (2003) examined the role of this lateral Poincaré wave shear in smaller lakes, and found that it was the mechanism expected to dominate dispersion. In larger lakes, however, the lateral shear associated with internal Poincaré waves is negligible because of the basin size, and lateral shear flow dispersion from the wave would not be expected to play a large role in lateral dispersion.

Our work here examines the hypothesis that in very large basins, the vertical shear associated with near-inertial internal Poincaré waves will enhance lateral dispersion. The outline of this article is as follows. In the Methods section, we present field measurements from Lake Michigan's southern basin, and describe the mixed layer turbulence and dispersion quantification techniques (K-profile turbulence parameterization and numerical particle tracking, respectively). In the Results section, we highlight the vertical and temporal structure of currents and turbulence in the mixed layer, and present particle tracking calculations that quantify the effect of the currents and turbulence on lateral dispersion. In the Discussion section, the characteristics of estimated horizontal dispersion and vertical mixing in the surface layer are discussed relative to standard diffusion diagrams, and simple parameterizations are proposed to characterize the shear effect on dispersion.

Methods

Analytical solutions for oscillating shear

As a model problem describing the shear flow dispersion enhanced by the vertical shear of internal Poincaré waves, we revisit the work of Smith (1982), and more recently Steinbuck et al. (2011), who examined idealized 2-D oscillatory shear flow dispersion, both in the context of oceanic internal wave-enhanced dispersion. We consider substances released into, and confined to, a mixed layer of thickness H, with a linear current shear U/H (U = maximum velocity difference) over the mixed layer, and a vertical mixed layer diffusion coefficient K_z (Fig. 1). The current field oscillates in time with wave period T. After the diffusion time $T_d \equiv H^2/K_z$, a state of shear flow dispersion will be achieved (Taylor 1953, 1954), and the lateral variance of the cloud in the flow direction will grow linearly with time, with a cycle-averaged (irreversible) dispersion coefficient K given by:

$$K = \frac{K_z}{\pi^4} Pe^2 T_*^2 \sum_{n=1}^{\infty} (2n-1)^{-2} \left\{ \left[\frac{\pi}{2} (2n-1)^2 T^* \right]^2 + 1 \right\}^{-1} \quad (1)$$

(Holley et al. 1970; Fischer et al. 1979). While perhaps not obvious, Eq. 1 demonstrates that the effect of unsteadiness on lateral shear flow dispersion is always to reduce the dispersion coefficient from the equivalent steady value ($K_{steady} = \frac{U^2 H^2}{120 K_z}$), with the exact reduction dependent on the various timescale ratios in the problem.

Following Steinbuck et al. (2011), the solution (Eq. 1) is best described in terms of the governing timescales and their ratios, with the timescales of advection ($T_a = H/U$), diffusion ($T_d = H^2/K_z$), and wave period (T) forming nondimensional timescale ratios of $Pe \equiv \frac{T_d}{T_a} = \frac{UH}{K_z}$ and $T^* \equiv \frac{T}{T_d} = \frac{TK_z}{H^2}$. Thus, the nondimensional dispersion rate KK_z^{-1} can be expressed in terms of the Peclet number (Pe) and T^*, implying that KK_z^{-1}, the ratio of the horizontal dispersion rate to the vertical mixing rate, increases as T_a or T increases relative to T_d.

For quasi-steady flow, i.e., long wave periods relative to a fast diffusion time scale, $T^* \gg 1$, a result similar to Taylor's classic steady flow result is recovered when time t is larger than T_d, for which the lateral dispersion coefficient is inversely proportional to the diffusion coefficient, and equal to one half of the corresponding steady case:

$$K = \frac{U^2 H^2}{240 K_z} \quad (t > T_d). \quad (2)$$

In the opposite limit, when turbulent diffusion is slow relative to the wave period ($T^* \ll 1$), the cycle-averaged dispersion coefficient for times greater than the diffusion time is directly proportional to the turbulent diffusion coefficient:

$$K = \frac{U^2 T^2}{8\pi H^2} K_z \quad (t > T_d). \quad (3)$$

For fixed U, H, and T, the dispersion coefficient will be maximized when the diffusive and wave time scales are comparable ($T^* = 0.63$), and in this case the "optimal" lateral dispersion rate is $K = \frac{U^2 T}{302}$. Figure 1 illustrates some representative solutions showing the effect of the timescale ratios on the lateral dispersion rate.

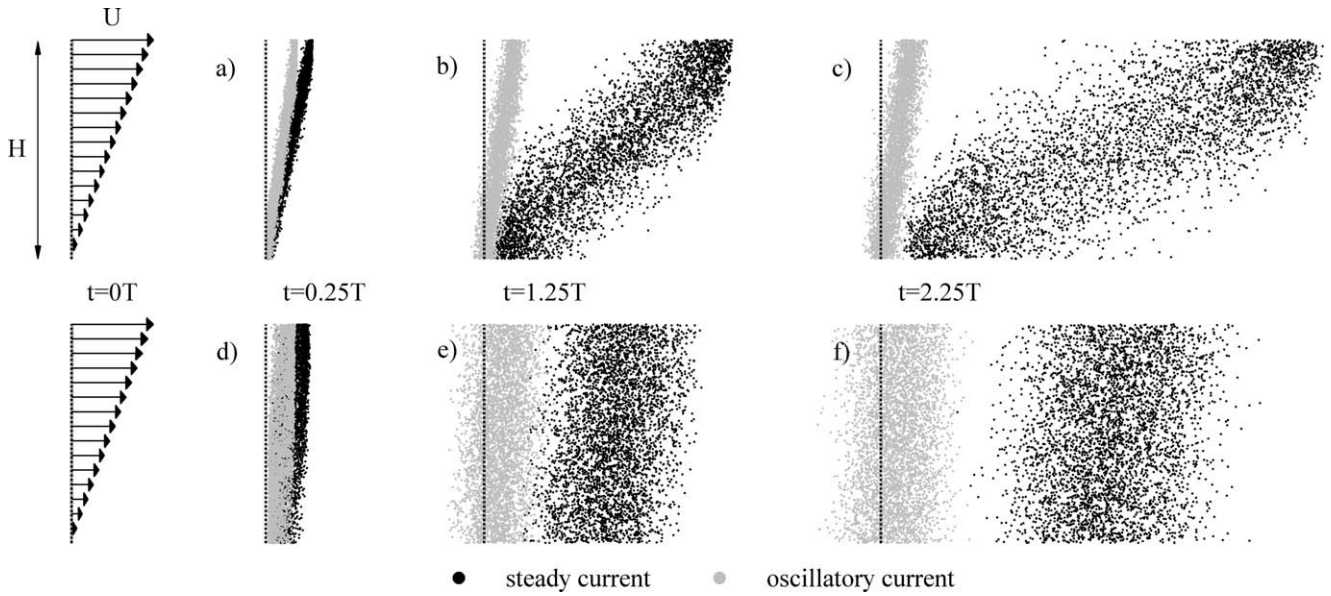

Fig. 1. Shear flow dispersion of released particle lines in idealized steady (black particles) and oscillatory (gray particles) currents at $t = 0$, 0.25 T, 1.25 T, and 2.25 T, where $T = 18$ h. Upper panels (a-c) display shear flow dispersion with $K_z = 0.0001$ m^{2}s^{-1} and $T^* = 0.028$ ($T_d = 26$ d), and lower panels (d-f) display shear flow dispersion with $K_z = 0.0023$ m^{2}s^{-1} and $T^* = 0.63$ ($T_d = 1.13$ d). The maximum current is 0.2 ms^{-1} and depth is 15 m. Reflective boundary conditions are applied on upper and lower boundaries.

Thus, the effect of vertically sheared, oscillating currents on lateral dispersion is highly dependent on the advection (T_a), oscillation (T), and vertical mixing timescales (T_d). The advection and wave timescales associated with near-inertial internal waves for the mixed layers of large temperate lakes and mid-latitude oceans do not vary widely ($T_a \equiv \frac{H}{U} \sim \frac{10\ m}{10^{-1}\frac{m}{s}} \sim\ 10^2$ s and $T \sim \frac{1}{f} \sim 10^4$ s, respectively). However, in the mixed layer the vertical mixing timescale T_d can vary by many orders of magnitude with varying surface forcing, and hence the vertical mixing coefficient, and its temporal distribution, are particularly important components of the mixed layer dispersion problem. In large lakes, mixed layer turbulence during the stratified period is driven primarily by the wind and velocity shear, and heavily modified by thermal stratification. Measurements suggest that the typical values of vertical diffusivity in the mixed layer of large lakes are of order $K_z \sim 10^{-5}-10^{-2}$ m^2 s^{-1} (Wüest et al. 2009), yielding diffusion timescales of $T_d \equiv \frac{H^2}{K_z} \sim 10^4 - 10^7$s, i.e., hours to months. Moreover, the solution (Eq. 1) may not ever be applicable when vertical diffusion is weak, as it is for times much greater than the diffusion time, when the dispersion has reached a quasi-steady state. As such, it is difficult to generalize the effect of near-inertial internal waves on mixed layer dispersion a priori, without an exact estimation of the various timescales involved in the problem, and direct calculations of shear flow dispersion.

For the present problem of internal Poincaré wave-induced oscillatory currents, the vertically sheared currents are additionally rotating anti-cyclonically, i.e., co-oscillating in both lateral directions. In this case, provided that the oscillating flow does not vary laterally, dispersion becomes radially symmetric, with the radial dispersion coefficient given by Eq. 1 for times greater than the diffusion times. Note that while the rate of dispersion is the same between the 2-D and rotating shear cases, the rotating Poincaré case accomplishes more dilution because of the radially symmetric spread, i.e., the shear flow dispersion is not simply occurring along a single direction.

Field measurements

Measurements of full water column temperatures and current velocities were obtained at a mooring in 151 m water

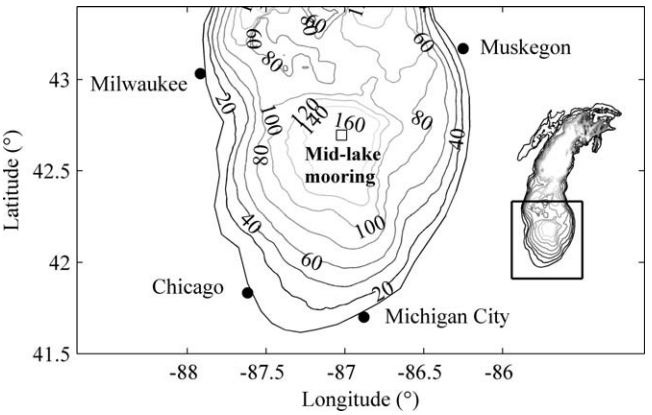

Fig. 2. Location of mid-lake mooring in southern Lake Michigan, with depth contours shown in *m*.

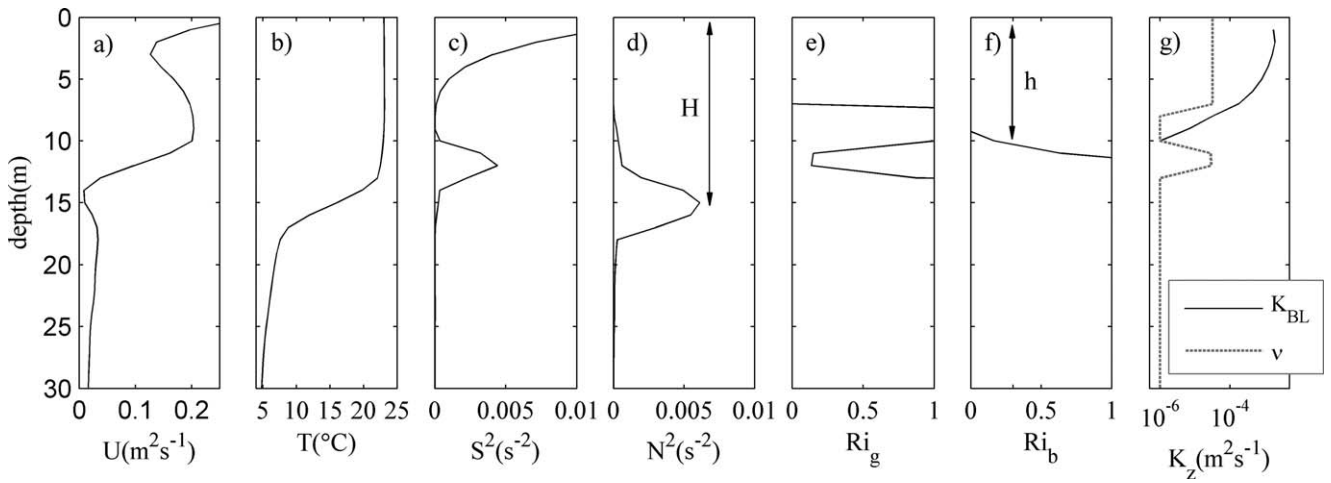

Fig. 3. Observations and calculated vertical diffusivity estimated by the KPP model on DOY 234.: (**a**) speed; (**b**) temperature; (**c**) shear $S^2=(\partial u/\partial z)^2+(\partial v/\partial z)^2$; (**d**) Buoyancy frequency $N^2=-g/\rho_0\ \partial\rho/\partial z$; (**e**) gradient Richardson number; (**f**) bulk Richardson number; (**g**) the vertical mixing coefficients $K_{BL}(m^2s^{-1})$ and $\nu(m^2s^{-1})$ calculated by KPP. H(m) and h(m) indicate mixed layer and boundary layer depths, respectively.

depth near the center of Lake Michigan's southern basin (Fig. 2), which is a location where internal Poincaré waves have maximum influence on surface and mixed layer currents (Choi et al. 2012; Ahmed et al. 2013). We utilize a full year record of measurements, collected between DOY 127 on 2003 and DOY 127 on 2004 (DOY = day of year), but focus primarily on the stratified period of 2003. A pair of upward- and downward-looking acoustic Doppler current profilers (ADCP's) provided hourly measurements in 4 m bins between 6 m and 40 m depth, and in 8 m bins from 59 m to 140 m depth. Currents in the top 5 m were extrapolated with a spline scheme. A total of 11 temperature loggers attached to the mooring between 7 m and 147 m depth measured water temperatures each hour. Standard meteorological and water surface temperature data was obtained from a nearby NOAA NDBC buoy (45007). Heat flux estimates were obtained from the National Centers for Environmental Prediction – North American Regional Reanalysis (NCEP – NARR) dataset provided by the NOAA/MAR/ESRL PSD, Boulder, Colorado, from their Web site at http://www.esrl.noaa.gov/psd/.

Particle tracking

We employ numerical particle tracking to quantify the effect of ADCP-observed velocity shear on lateral dispersion, following work by Steinbuck et al. (2011). For this technique, clouds of particles are tracked, with their motion given as a combination of advection (deterministic; specified by the ADCP fields) and turbulent diffusion (stochastic; parameterized with a turbulence model). In the ensemble limit of many such particles, the statistics of the particle position distributions approach the analytical solutions to the advection-diffusion equation (Ross and Sharples 2004). Following Visser (1997), particle advection and diffusion from the present location x_i to the new location x_{i+1} over a time-step dt is given by:

$$x_{i+1}=x_i+u_i dt+\frac{\partial D_i}{\partial x_i}dt+R\sqrt{2r^{-1}D_i^* dt}, \quad (4)$$

where D_i indicates the present diffusivity at x_i, and D_i^* indicates the present diffusivity at position $x_i+1/2(\partial D_i/\partial x_i)dt$. R is a uniformly distributed random number, and $r=1/3$ (Visser 1997).

Equation 4 was employed in three dimensions to track clouds of surface-released particles released continuously throughout the measurement period. The particle tracking code was validated against known shear flow dispersion formulas (e.g., Eq. 1 and other results from Fischer et al. (1979) and Smith (1982)). Clouds of 4,000 particles were released every 6 h throughout the measurement period at the water surface, and tracked for 7 d.

Advection was specified according to the particle locations (depth and time) in the vertically and temporally interpolated ADCP velocity fields; diffusion was specified according to estimated diffusivities given by the K-profile parameterization turbulence model, which is described in the subsequent section. We treated the ADCP-derived velocity fields used for advection as being horizontally uniform over 7 d. The average calculated cloud size (3σ, where σ is the standard deviation of the particles' lateral positions) and average cloud displacement after 7 d were 11.9 km and 15.0 km, respectively, i.e., much smaller than the basin size ($\sim$ 135 km), which is the scale over which the induced internal Poincaré wave velocities vary; this suggests that the laterally uniform current assumption was reasonable.

To quantify the particle cloud size, the standard deviations of the particle displacements in the East-West and North-South directions were calculated for each time step, and the eigenvalues and eigenvectors of these deviations

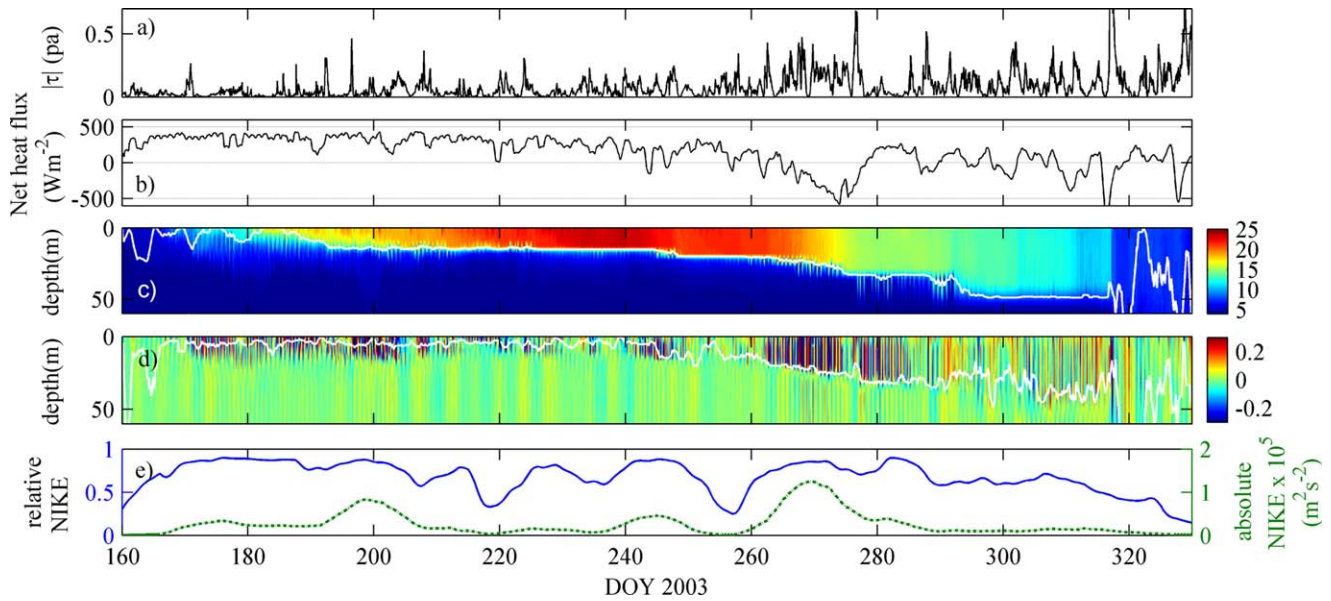

Fig. 4. Raw measurements from Lake Michigan mid-lake mooring (2003): (**a**) magnitude of wind stress; (**b**) estimated net incoming heat flux; (**c**) water temperature and the location of maximum N^2 (white line); (**d**) observed EW velocity and location of maximum S^2 (white line), and (**e**) absolute (dotted line) and relative (%, solid line) near-inertial kinetic energies (NIKE) at 10 m depth.

were used to convert to standard deviations in the major (σ_i) and minor (σ_j) axes, following Okubo (1971). Both reversible and irreversible dispersion were tracked for the particle clouds, following Sundermeyer and Ledwell (2001). Two definition of the dispersion coefficient were considered: $K_t = \frac{1}{4}\frac{\sigma_r^2}{t}$ (Okubo 1971; $\frac{1}{2}\frac{\sigma_r^2}{t}$ in Steinbuck et al. 2011), an integrated measure of dispersion over the time since release t; and $K = \frac{1}{2}\frac{\partial \sigma_r^2}{\partial t}$, an instantaneous rate of spreading, where σ_r^2 is the radially symmetrical variance $\sigma_r^2 = 2\sigma_i\sigma_j$. To facilitate comparison with published mixed layer dye release experiments (Okubo 1971; Murthy 1976), we use the former definition in this article (unless otherwise stated).

Vertical mixing parameterization

To estimate turbulent diffusion coefficients within the surface mixed layer and thermocline, we employ the K-profile parameterization (KPP; Large et al. 1994, to which the reader is referred for full details), which has been used successfully in simulating turbulence in lake and oceanic mixed layers (e.g., Zedler et al. 2002; Huang et al. 2010). The KPP model consists of two schemes: a surface boundary layer scheme and an interior scheme. The interior scheme calculates the interior vertical diffusivity v, and the boundary layer scheme calculates the surface boundary layer diffusivity K_{BL}. A sample calculated turbulent diffusion profile from the ADCP and temperature data is presented in Fig. 3.

The maximum vertical diffusivity induced by interior shear mixing was set as $v_0 = 3.1\times10^{-5}$ m^2s^{-1} which is the maximum vertical diffusivity measured in the thermocline in Lake Erie in July (Bouffard et al. 2012). We chose $v_b = 10^{-6}$ m^2s^{-1} as background vertical diffusivity, which is a typical value observed in the lake hypolimnion (Wüest et al. 2009). The diffusivity v is set to v_0 below the mixed layer depth H, which is defined as the location of maximum N^2.

The enhanced vertical diffusivity associated with surface waves was added following the approach of Huang and Qiao (2010) to the KPP-modeled vertical diffusivity, but this component was found to have a negligible effect on the calculated vertical mixing and lateral dispersion. This is not entirely unexpected as the stratified period is the period of weakest winds for Lake Michigan, and Lake Michigan has a modest fetch relative to oceanic systems.

Results

Dominance of near-inertial Poincaré waves

The basic measurements are presented in Fig. 4, which shows the seasonal evolution of wind stress, net surface heat flux, water column temperatures, and currents. As is typical for Lake Michigan, thermal stratification starts in May and develops through November with a steadily deepening mixed layer through the summer and fall. We consider two time periods, an early stratified period (DOY 170−240) and a later stratified period (DOY 240−310), separated by the time of maximum stratification, i.e., maximum Burger number (DOY 240). The basic characteristics of the two periods are described in Table 1. Wind is relatively weak in the early stratified period, while in the later stratified period stronger winds usually accompany negative surface heat flux and mixed layer deepening. Generally speaking, during the early stratified period the surface layer can be characterized as having stronger shear and stratification over the surface layer

Table 1. Comparison of observations and calculations in early and later stratified periods.

	Early period (DOY 170–240)	Late period (DOY 240–310)
Surface stability*	Neutrally stable and stable	Frequently unstable
Stratification	Weakly and strongly stratified surface layer	Well-mixed surface layer; stratification confined to thermocline
Shear	Strong shear in the surface layer	Weak shear in the mixed layer and strong shear in the thermocline
Average wind stress (Pa)	0.039	0.057
Average mixed layer depth H (m)	11.4	30.8
Near-inertial Kinetic energy at 10 m depth	74% (relative) 2.6×10^4 m^2s^{-2} (absolute)	70% (relative) 3.4×10^4 m^2s^{-2} (absolute)
$3\sigma_r$ after 7 d (km)	13.61	15.76
Lateral dispersion coefficients		
K_{9h}†	1.64 (0.91)	1.50 (0.90)
K_{3d}†	5.84 (4.19)	8.28 (7.89)
K_{7d} (m^2s^{-1})†	9.03 (3.83)	12.72 (8.64)
Log-average vertical mixing coefficient over the mixed layer K_z (m^2s^{-1})‡	2×10^{-5} (1.29×10^{-4})	2.90×10^{-3} (4.2×10^{-3})

*Determined by Monin–Obukhov length scale.
†Median and standard deviation (in parentheses).
‡Standard deviation is indicated in parentheses.

(which is not that well mixed), while during the later stratified period the surface layer can be characterized as well-mixed, having weak shear, with strong stratification and shear concentrated in the thermocline below.

As we have shown previously for other years (Choi et al. 2012 for 1998–1999), near-inertial energy (here defined as energy extracted from the 15 h to 20 h band-pass filter) in the mixed layer is seen to regularly comprise more than 80% of the observed total kinetic energy in the surface layer at this location (Figs. 4e, 5). Bursts of near-inertial energy occur following wind events, with decay scales of 7–10 d; near-inertial activity ceases only following whole water column homogenization in early winter. Clear near-inertial periodicity is seen in the raw ADCP data, with oppositely directed velocities above and below the thermocline that are suggestive of vertical mode 1 structure (Fig. 4d). The vertical structure in the velocities evolves seasonally with the stratification, with the zero crossing location following the base of the mixed layer.

Complex empirical orthogonal function (EOF) analysis performed on the observed currents shows that the dominant vertical structure of the currents closely matches the lowest baroclinic mode predicted by standard normal modes analysis (e.g., Kundu et al. 2012; Fig. 6). The dominant vertical EOF mode, which can be shown spectrally to be associated with the near-inertial internal Poincaré wave, rotates clockwise at near-inertial period as expected, and is regularly responsible for more than 80% of the observed variance in the vertical profiles. This analysis suggests that, to a very good approximation, the flow at this location can be approximated as having vertical mode 1 structure—set by the thermal stratification via the usual normal modes formulation—that continuously rotates clockwise at a near-inertial period.

As is typically the case per the normal modes solution, the vertical mode 1 structure is seen to mirror the stratification; in the early stratified period, when stratification exists throughout the surface layer, mode 1 shows shear existing throughout the surface layer. Later, when the mixed layer is fully developed and stratification exists only in the thermocline, mode 1 shear is also concentrated at the thermocline. The complex EOF analysis also shows that when stratification exists in the near-surface layer, the dominant (mode 1) mode shows spiraling throughout the surface layer where stratification exists (Fig. 6c); this spiraling is not captured by the normal modes analysis, which is 2-D. The spiraling may be indicative of shear-generated turbulence leading to friction and an Ekman-like spiral.

Vertical mixing

Figure 7 shows the mixed layer vertical diffusivity distribution calculated by the KPP turbulence model. The model calculates a depth averaged surface layer vertical diffusivity that grows over the stratified period from 10^{-5} m^2s^{-1} at the onset of stratification to 10^{-3} m^2s^{-1} at the end of the stratified period when the fall overturn is nearly complete. These mixing rates are consistent with recent summertime

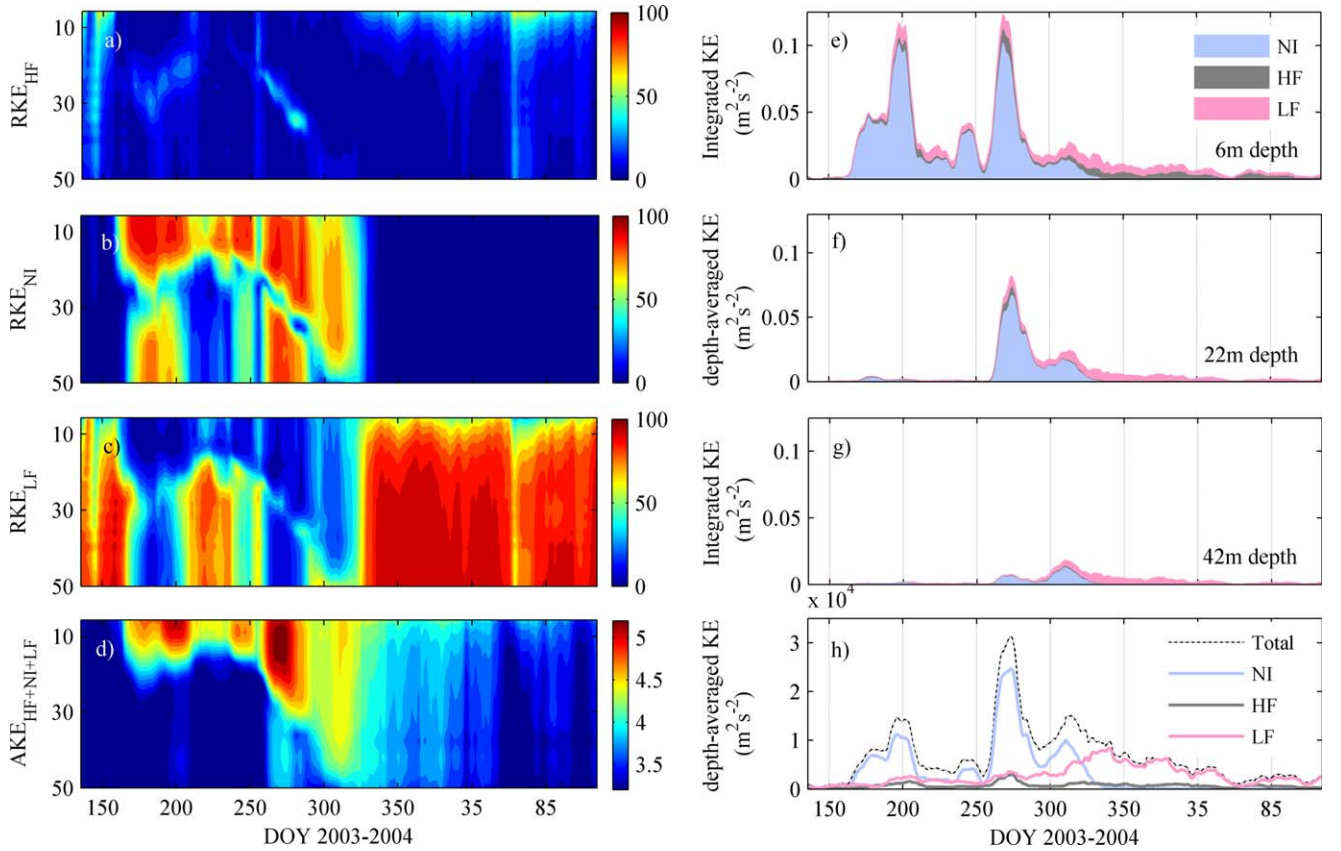

Fig. 5. Spatial and temporal variation of kinetic energy spectrum: (**a**)–(**c**) relative kinetic energy in HF (0–15 h), NI (15 – 20 h), and LF (>20 h) filtered currents; (**d**) absolute kinetic energy (m^2s^{-2}) of combined current in log_{10}-scale; (**e**)–(**g**) integrated kinetic energy at 6 m, 22 m, and 42 m depth; (**h**) depth-averaged (whole water column) kinetic energy obtained from (**a**)–(**d**).

measurements in Lake Erie (Bouffard et al. 2012). Corresponding vertical mixing timescales for the mixed layer range from order of 1 to 600 d. Thus, the entire record has the estimated vertical mixed layer mixing timescale greater than the inertial period (18 h), with T_*=0.158 (averaged, 0.051 and 0.247 for early and later stratified periods).

The calculated seasonal variation in mixed layer mixing rates occurs in response to the wind stress and boundary layer depth increasing through this period (Fig. 8). In the early stratified period, weak wind and the shallow boundary layer depth do not allow significant vertical mixing. The daily-depth-averaged K_z for the mixed layer remains at order 10^{-5} m^2s^{-1} for u^*h (h = boundary layer depth) smaller than 0.01 m^2s^{-1}, in which case the turbulence model predicts that the wind can not effectvely penetrate the surface stratification. For $u^*h > 0.01$ m^2s^{-1}, the average mixed layer K_z roughly follows a $(u^*h)^{3/2}$ dependence with the estimated log-averaged mixed layer diffusivity being reasonably approximated as $K_z = (1/15)(u^*h)^{3/2}$, with K_z and u^*h in m^2 s^{-1} (Fig. 8).

Analysis of the various components in the turbulence model shows that in the early stratified period, the main forcing for the vertical mixing in the stratified surface layer is a shear-induced hydrodynamic instability related to the local gradient Richardson number condition. During this period, the water column stratification extends almost to the lake surface, which in turn creates substantial shear over the near-surface layer per the normal modes solutions as described earlier. In the later stratified period, the main forcing for the vertical mixing in the surface layer is direct wind-induced turbulence related to the nonlocal bulk Richardson number. Also during this later period, shear is concentrated at the base of the mixed layer and serves to enhance turbulence there.

Lateral dispersion rates

Figure 9 shows the radially symmetrical variance σ_r^2 and the dispersion coefficient $K = \frac{1}{4}\frac{\sigma_r^2}{t}$ (Okubo 1971) as calculated from the particle tracking. Median standard deviation calculated dispersion coefficients are given in Table 1 in which K_{9h}, K_{3d},and K_{7d} are the dispersion coefficients measured at 9 h ($=T/2$), 3 d, and 7 d following release. The largest K_{7d} is about 40 m^2s^{-1} observed between DOY 260 and 280 when wind stress and near-inertial energy is high, and the lowest lateral dispersion rate is about 0.1 m^2s^{-1} observed in the early stratified period when surface stratification is strong.

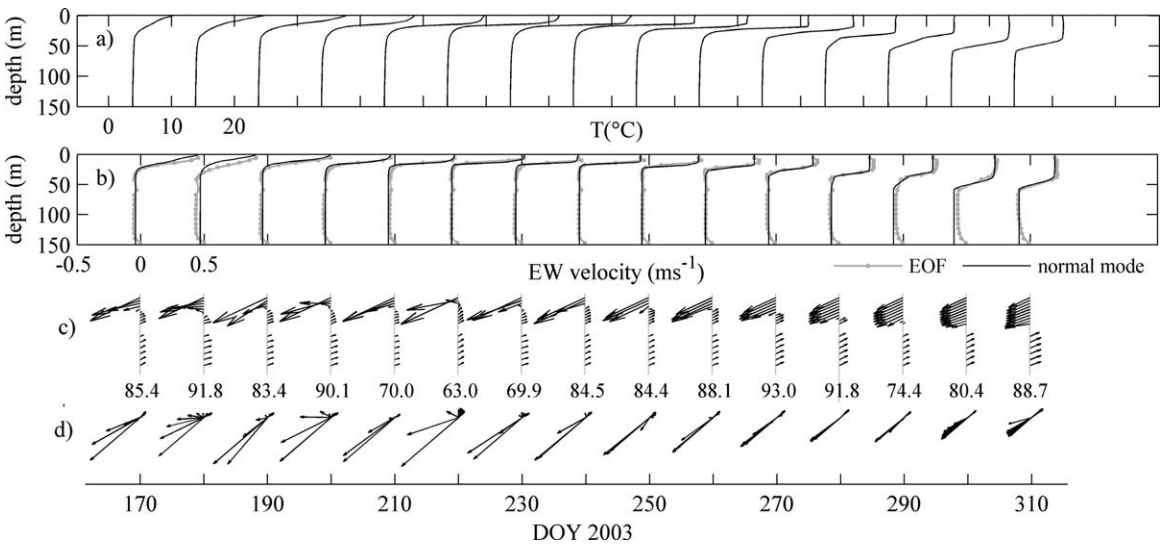

Fig. 6. (**a**) Measured 10 day-averaged temperature profiles; (**b**) normal mode solutions (black line) and 1st EOF mode of EW velocity (gray line); (**c**) 2-D velocity profile of 1st complex EOF mode of EW velocity. % variance for individual 1st EOF mode is indicated below each profile; (**d**) projection of the velocity vectors to show spiraling. Each EOF profile used a 10 d window for calculation. The first and last profiles correspond to DOY 170 and 310, respectively, and intervals between profiles are 10 d.

These values are comparable to the few surface layer dispersion measurements performed in the Laurentian Great Lakes (Csanady 1963, 1964; Huang 1971; Murthy 1976), and we further this comparison later in the manuscript. In all cases, the lateral dispersion rate is significantly larger than the vertical mixing rate, which is a consequence of the vertical shear driving the dispersion in the calculation, and the relatively low vertical mixing rates in the mixed layer.

We calculate the highest lateral dispersion rates when vertical mixing is strongest. This relationship is consistent with the analytical solution (Eq. 3) for $T^* < 1$, i.e., sub-inertial currents dominating dispersion. The largest K found occurs during DOY 260–280, and in this time period, the elevated dispersion in the mixed layer was bolstered by strong shear and a strong vertical mixing coefficient (Fig. 12), the latter of which was sustained by strong wind and negative surface heat flux (Fig. 4). The negative heat flux increases K_z because

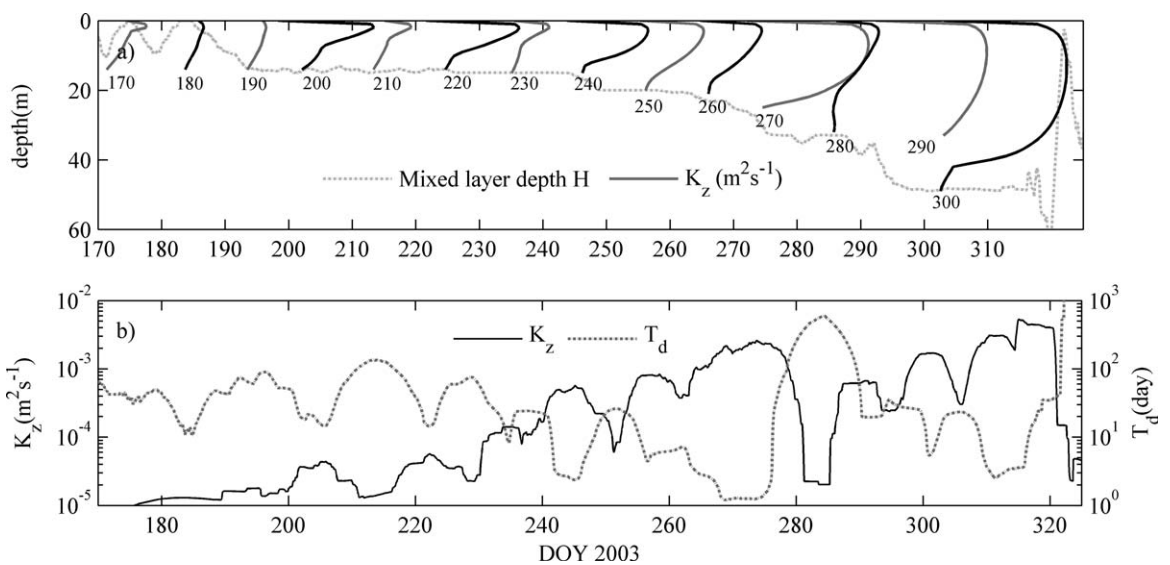

Fig. 7. Vertical turbulent diffusivities as estimated by the modified KPP model: (**a**) daily averaged vertical diffusivity distribution, shown every 10 d (solid lines) and mixed layer depth (dotted line). K_z profiles have been drawn here as $\log_{10}$-scale plots associated with their respective DOYs (indicated by numbers below each profile), and corresponding DOY in x-axis indicates $10^{-6}m^2s^{-1}$ with the DOY+10 indicating $10^{-4}m^2s^{-1}$; (**b**) $\log_{10}-3$ days-depth-averaged diffusivity and diffusion time T_d in the mixed layer.

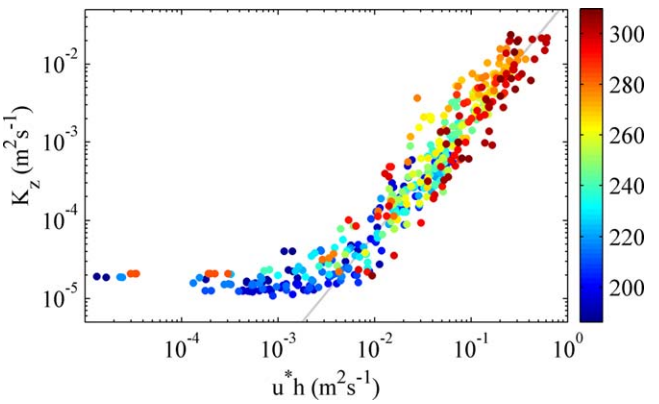

Fig. 8. Correlation between K_z (m^2s^{-1}) and u^*h (m^2s^{-1}) obtained from the turbulence model. Each parameter is daily averaged. K_z is depth-averaged over the mixed layer. The data points are colored by DOY. The gray reference line indicates $K_z = 1/15\ (u^*h)^{3/2}$.

the turbulent velocity scale is associated with heat flux via the Monin–Obukhov length scale. The temporary formation of surface restratification, e.g., DOY 280−285, results in temporal decreases in vertical transport of particles (Fig. 9c).

Different characteristics of lateral dispersion are observed in early and later stratified periods (Fig. 9; Table 1), which can be explained by the differing thermal and shear structure for those periods. Strong near-surface shear in the early stratified period does not result in enhanced lateral dispersion because near-surface stratification suppresses the wind- and shear-induced vertical mixing. Weak near-surface shear in later stratified period effectively enhances lateral shear dispersion because the mixed layer is vulnerable to stronger later-stratified period wind that enhances vertical mixing. Consequently, the later stratified period provides the most favorable environment for lateral shear dispersion once wind-induced shear and vertical mixing cooperate in the mixed layer.

Discussion

Dominant current driving dispersion

To better understand the role of near-inertial shear on lateral dispersion, we additionally carried out numerical particle tracking calculations using band-passed ADCP data for three separate spectral bands: high frequency band (HF, below 15 h), near-inertial frequency band (NI, 15–20 h), and low frequency band (LF, above 20 h). The HF current band, as defined, includes barotropic seiches and higher-frequency internal waves, and the LF current band includes sub-inertial basin-scale motions and near-surface shear developed by persistent (sub-inertial) winds. Figure 10 illustrates the filter characteristics as applied to the measured velocities, showing that the filter effectively isolates the broad near-inertial peak associated with low-mode internal Poincaré waves. Additional calculations with the near-inertial band defined as a broader band (10–25 h) yielded nearly identical results, suggesting that the results are not dependent on the particular filter characteristics.

The results of the particle tracking performed on the filtered currents demonstrate that near-inertial shear dominates the calculated lateral dispersion up to times comparable to the inertial wave period, but sub-inertial shear

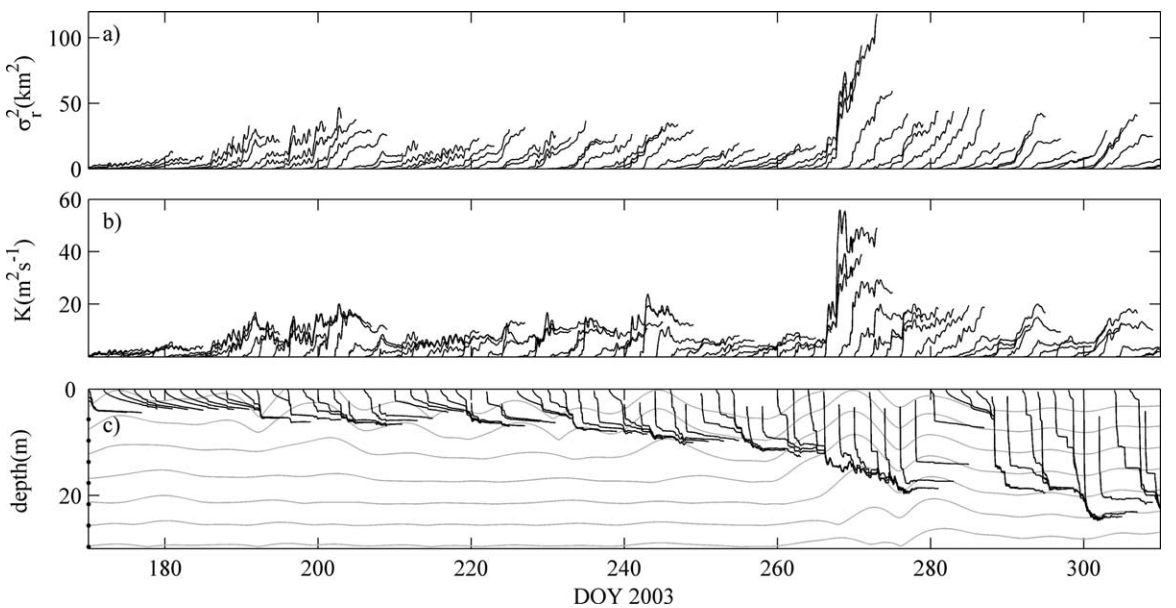

Fig. 9. Results of data-driven particle tracking models (irreversible dispersion), showing cluster behavior for clusters release every 2 d: (**a**) lateral variance of particle displacement; (**b**) dispersion coefficient; (**c**) mean location of particle cluster. The black lines in (**c**) indicate Hilbert envelops of near-inertial filtered current at various depths, and dots in the *y*-axis indicate zeros for each line. 10 m depth corresponds to 50 cms^{-1}.

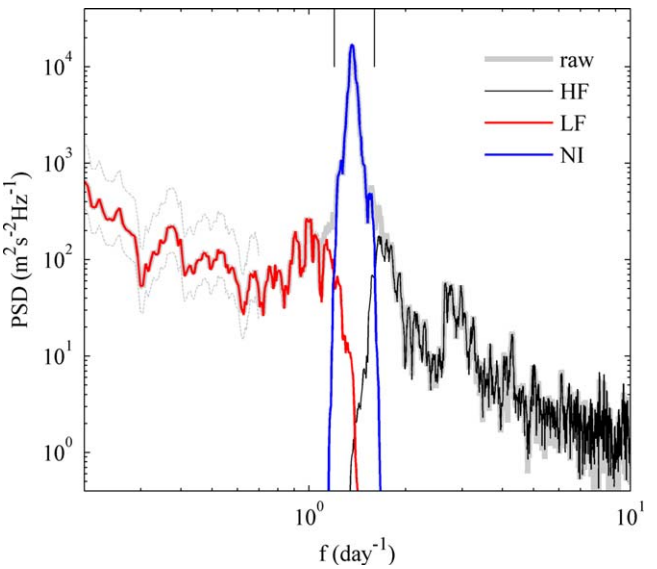

Fig. 10. Power spectral density for east-west velocity measured during DOY 170–310 at 10 m depth. Also shown are spectra of filtered currents (HF: period < 15 h, NI: 15 < period < 20 h, and LF: 20 h < period) examined in the particle tracking exercises, and confidence intervals as faint gray lines at left of plot. The frequencies corresponding to 15 h and 20 h are indicated by vertical lines.

dominates the lateral dispersion for longer time periods (Figs. 11, 12).

The effect of near-inertial shear on dispersion is also seen to have an important role in setting the time behavior of the plume spreading, with different spreading rates before and after the inertial period (Fig. 11). The NI current-driven dispersion shows that the lateral dispersion coefficient is proportional to $L^{4/3}$ before the inertial timescale T, after which it follows Fickian behavior with the constant, but enhanced dispersion coefficient order of 1 m^2s^{-1}. The maximum lateral dispersion coefficient driven by LF current is order of 10 m^2s^{-1}, and roughly follows $L^{4/3}$ (Fig. 11).

Thus, sub-inertial shear appears to dominate lateral dispersion except for times less than the inertial period, despite near-inertial kinetic energy thoroughly dominating the spectrum. This effect of LF shear on lateral dispersion can be explained with some of the timescale arguments described previously. For $T^* < 1$, Eq. 3 states that the lateral dispersion in an oscillatory current is enhanced as the timescale of the unsteadiness increases, and thus it is expected that lower-frequency shear will be more effective at shear flow dispersion.

The high-frequency current was found to provide a negligible contribution to lateral dispersion. The HF current-driven dispersion roughly follows Fickian behavior with dispersion coefficient order of 0.1 m^2s^{-1}.

Dispersion parameterizations

Of much utility are simple parameterizations for the dispersion coefficient in terms of readily observed physical parameters, such as the water surface current U_{surf}, mixed layer depth, and/or wind stress. We attempted to develop empirical parameterizations linking the calculated 7 d dispersion coefficient K_{7d} to the dimensional parameters u^*, U_{surf}, K_z, and H. Here $u^* = \sqrt{\tau/\rho_w}$ is the water friction velocity associated with the wind stress, where τ is the wind stress and ρ_w is the surface water density and U_{surf} is the water surface velocity. We found reasonably simple relationships between the non-dimensional dispersion rate $K_{7d}K_z^{-1}$ with the Peclet numbers Pe $(=U_{surf}HK_z^{-1})$ and Pe^* $(=u^*HK_z^{-1})$, with $K_{7d}K_z^{-1}$ having approximately linear relationships with Pe and Pe^* (Fig. 13). All parameters except K_{7d} are averaged over the 7 d. The Peclet numbers indicate the ratio of the rate of advective transport driven by characteristic velocities U_{surf} and u^* to the rate of turbulent diffusive transport. The Peclet numbers generally increase with time over the stratified period,

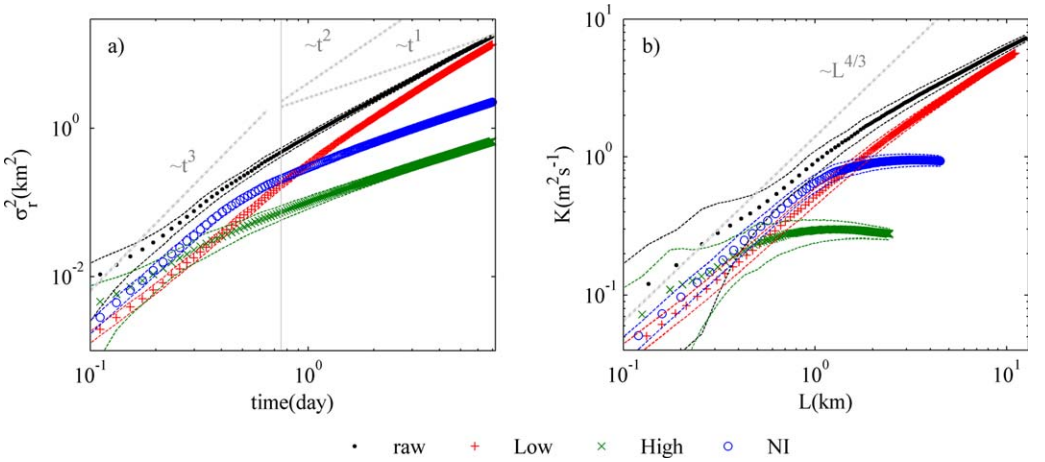

Fig. 11. Diffusion diagrams based on particle tracking model: (**a**) Variance σ_r^2 vs. time with grey reference lines indicating $\sigma_r^2 \sim t^1$, t^2, and t^3; (**b**) dispersion coefficient K vs. size of plume L with grey reference line indicating $K \sim L^{4/3}$. Dashed lines are 95% confidence intervals.

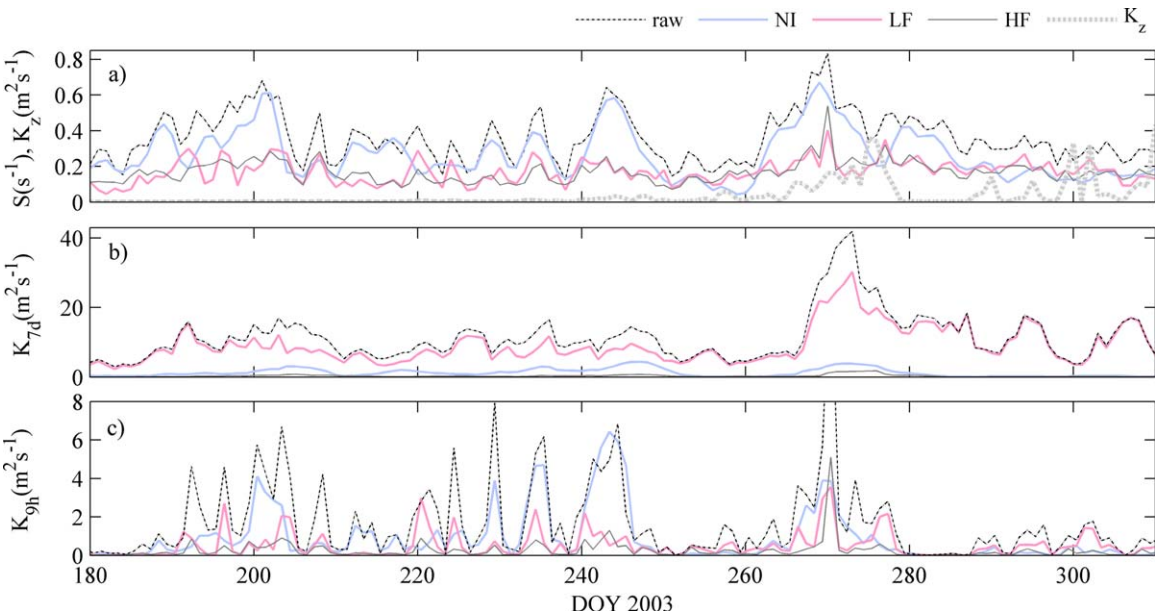

Fig. 12. (**a**) Depth averaged shear S for filtered LF, NI, and HF currents and depth averaged K_z within mixed layer depth; (**b**) dispersion coefficient measured at 7 d (K_{7d}) for raw and filtered currents; (**c**) dispersion coefficient measured at 9 h (K_{9h}) for raw and filtered currents.

as wind stress, surface currents, and the mixed layer depth increase. From a simple regression, K_{7d} can be expressed as a simple dimensional formula that allows for a straightforward estimate from measurements:

$$K_{7\mathrm{d}} \cong 2.4\ U_{\mathrm{surf}}H \cong 66\ u^*H \tag{5}$$

Although the theoretical non-dimensional dispersion rate KK_z^{-1} for sheared oscillatory current depends on both Pe and T^* (Eq. 1), the dispersion rate $K_{7d}K_z^{-1}$ can be estimated solely by Pe, according to this parameterization. This emphasizes that the effect of near-inertial waves on horizontal dispersion, which can be represented in terms of T^*, is hardly found at $t = 7$ d (this is maybe true even when t is greater than a few inertial periods).

It is worth noting that we do not observe large variations in the 7-d dispersion coefficient (Fig. 9), especially during the early stratified period, and thus the simplest possible parameterizations for the dispersion coefficients would be the seasonally dependent mean values provided in Table 1.

Diffusion diagrams

It is important to place the present results in the context of other published dispersion studies. The spreading rates of substances in oceans and large lakes are often characterized with size-dependent dispersion coefficients and time-dependent variances, with empirical observations and theories of the form:

$$\sigma_r^2 = at^m \tag{6}$$

$$K = c\sigma_r^n, \tag{7}$$

where $n = 2(m-1)m$. The classical Richardson's dispersion ($m = 3$ and $n = 4/3$) describes the spread of substances by eddies in the inertial subrange, in which case the dispersion coefficient is proportional to $\epsilon^{1/3}l^{4/3}$ (Batchelor 1950), where ϵ is dissipation rate of turbulent kinetic energy and $l = 3\sigma_r$ is horizontal length scale of the spreading plume. The $n = 4/3$ power law can be also be derived analytically for the case of unbounded shear flow dispersion (Saffman 1962), i.e., the early stages of shear flow dispersion for substances released from a boundary into a shear flow.

Observations of lateral dispersion in mixed layers have generally yielded values of $n \approx 4/3$ or less, e.g., 1.15 (Okubo

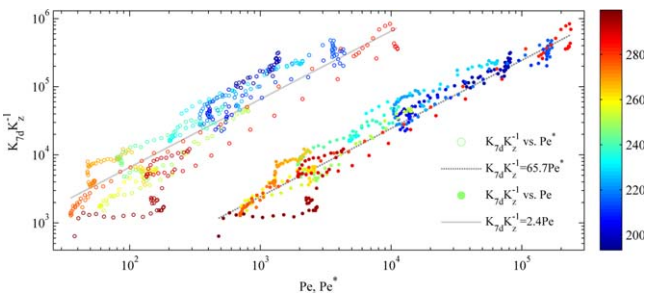

Fig. 13. Correlations between $K_{7d}K_z^{-1}$ and $U_{surf}HK_z^{-1}(=Pe)$, and $K_{7d}K_z^{-1}$ and $u^*HK_z^{-1}(=Pe^*)$ where U_{surf} is the near-surface current velocity magnitude extrapolated from ADCP measurements. Each parameter except K_{7d} is weekly averaged. The reference lines are obtained by line-fitting to linear equation in log-log scales. Data points are colored by DOY.

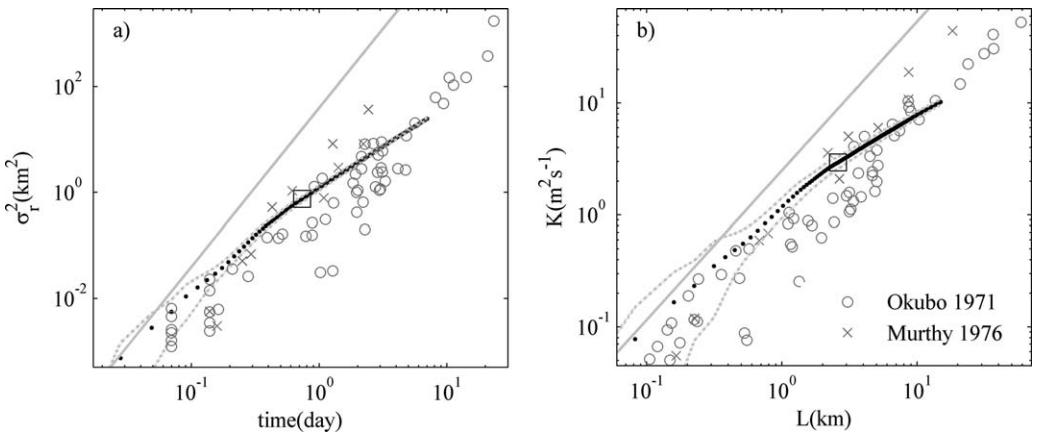

Fig. 14. Diffusion diagrams obtained from particle tracking model using raw current (black dots) and dye experiments in oceans and large lake ("o" and "x"). The dashed lines indicates 95% confidence intervals. R^2 between observations and our results are 0.82 (**a**) and 0.96 (**b**).

1971) and 1.33 (Kullenberg 1972) in oceans, 1.35 in Lake Ontario (Murthy 1976), 0.75 in a mid-sized lake (∼ 1 km; Peeters et al. 1996), and 1.1 in a small lake of order of 100 m (Lawrence et al. 1995).

The present results show size- and time-dependent dispersion coefficients that agree very well with the published data referenced above (Fig. 14), especially for the first several days of the calculations. This agreement demonstrates that unsteady shear flow dispersion is a plausible mechanism to explain observed dispersion rates in the mixed layers of oceans and large lakes, which is one of the key results of this article. It also shows that shear flow dispersion is another plausible explanation for observed $n = 4/3$ (Richardson) rates of dispersion, which can be explained by Saffman's (1962) unbounded shear flow dispersion result as discussed earlier. Conversely, however, our result does not prove that vertical shear flow dispersion is the mechanism responsible for the observed mixed layer dispersion rates, but it does show it to be a plausible explanation.

The "size-dependent" dispersion coefficients found here are better thought of as time-dependent dispersion coefficients, since the particle tracking calculations do not consider any lateral variability in the current fields causing the dispersion, and the particle clouds do not experience different types of current fields (eddy sizes) as their size increases. In contrast, this is a key ingredient in Richardson's 4/3 power dispersion, for the turbulence driving the dispersion is stationary. In the present case, the perceived dependence of the dispersion coefficient on cloud size is instead the effect of the unsteadiness of the sub-inertial currents driving the dispersion and the generally large diffusion timescales for the mixed layer; because these timescales are large relative to the timescales of interest (hours, days), the clouds never have enough time to reach the quasi-steady state of shear flow dispersion, at which point the present analysis should show a constant (size-independent, time-independent) dispersion coefficient for the remainder of the cloud spreading. Thus, our calculations show that because sub-inertial shear dominates dispersion in the mixed layer of Lake Michigan, clouds are generally still in the "early" stages of shear flow dispersion because of the large mixing times for the mixed layer.

The dispersion coefficients presented herein provide some target values for time-dependent simulated offshore dispersion rates of substances in the mixed layer of large lakes. These dispersion coefficients should not, however, be confused with lateral mixing coefficients specified in numerical models, which can be substantially smaller than these dispersion coefficients, provided the model faithfully represents the vertical structure of near-inertial and sub-inertial currents. Because the structure of this shear is largely set by the thermal structure, the ability of numerical models to accurately simulate lateral transport in large lakes may depend in large part on their abilities to resolve thermal structure; this is still a challenge for many large lake models (see, for example, Djoumna et al. 2014). Additionally, we see a great need for additional field data to validate dispersion models (both simple and complex). Complex transport models are becoming increasingly applied to a variety of settings, to simulate biological and chemical transport (e.g., Beletsky et al. 2007; North et al. 2008; Wynne et al. 2011; Dietrich et al. 2012). However, very little data exists to validate these modeling efforts, especially in the Laurentian Great Lakes, where complex ecological models are increasingly applied to inform management decisions for the lakes. To that end, several recent studies targeting coastal dispersion point to increased field efforts to aid in model validation (e.g., Wells et al. 2011; Thupaki et al. 2013), and it is our hope that this trend will continue, additionally targeting offshore waters long ago examined by Murthy (1976) and Okubo (1971).

References

Ahmed, S., C. D. Troy, and N. Hawley. 2013. Spatial structure of internal Poincaré waves in Lake Michigan. Environ. Fluid Mech. **14**: 1229–1249. doi:10.1007/s10652-013-9294-3

Antenucci, J. P., and J. Imberger. 2001. Energetics of long internal gravity waves in large lakes. Limnol. Oceanogr. **46**: 1760–1773. doi:10.4319/lo.2001.46.7.1760

Austin, J. 2013. Observations of near-inertial energy in Lake Superior. Limnol. Oceanogr. **58**: 715–728. doi:10.4319/lo.2013.58.2.0715

Batchelor, G. 1950. The application of the similarity theory of turbulence to atmospheric diffusion. Q. J. R. Meteorol. Soc. **76**: 133–146. doi:10.1002/qj.49707632804

Beletsky, D., D. Mason, D. J. Schwab, E. Rutherford, J. Janssen, D. Clapp, and J. Dettmers. 2007. Biophysical model of larval yellow perch advection and settlement in Lake Michigan. J. Great Lakes Res. **33**: 842–866. doi:10.3394/0380-1330(2007)33[842:BMOLYP]2.0.CO;2

Bouffard, D., L. Boegman, and Y. R. Rao. 2012. Poincaré wave-induced mixing in a large lake. Limnol. Oceanogr. **57**: 1201. doi:10.4319/lo.2012.57.4.1201

Choi, J., C. D. Troy, T.-C. Hsieh, N. Hawley, and M. J. McCormick. 2012. A year of internal Poincaré waves in southern Lake Michigan. J. Geophys. Res. Oceans **117**: C07014. doi:10.1029/2012JC007984

Csanady, G. 1963. Turbulent diffusion in Lake Huron. J. Fluid Mech. **17**: 360–384. doi:10.1017/S0022112063001403

Csanady, G. 1964. Turbulence and diffusion in the Great Lakes, p. 326–339. *In* Proceedings of the 7th Conference on Great Lakes Research.

Dietrich, J. C., and others. 2012. Surface trajectories of oil transport along the northern coastline of the Gulf of Mexico. Cont. Shelf Res. **41**: 17–47. doi:10.1016/j.csr.2012.03.015

Djoumna, G., K. G. Lamb, and Y. R. Rao. 2014. Sensitivity of the parameterizations of vertical mixing and radiative heat fluxes on the seasonal evolution of the thermal structure of Lake Erie. Atmos. Ocean **52**: 294–313. doi:10.1080/07055900.2014.939824

Fischer, H., E. List, R. Koh, J. Imberger, and N. Brooks. 1979. Mixing in inland and coastal waters. Academic Press.

Holley, E. R., D. R. Harleman, and H. B. Fischer. 1970. Dispersion in homogeneous estuary flow. J. Hydraul. Div. **96**: 1691–1709. doi:10.1061/JYCEAJ.0002160

Huang, A., Y. R. Rao, Y. Lu, and J. Zhao. 2010. Hydrodynamic modeling of Lake Ontario: An intercomparison of three models. J. Geophys. Res. Oceans **115**: C12076. doi:10.1029/2010JC006269

Huang, C. J., and F. Qiao. 2010. Wave–turbulence interaction and its induced mixing in the upper ocean. J. Geophys. Res. **115**: C04026. doi:10.1029/JC076i033p08147

Huang, J. C. K. 1971. Eddy diffusivity in Lake Michigan. J. Geophys. Res. **76**: 8147–8152. doi:10.1029/JC076i033p08147

Kullenberg, G. 1972. Apparent horizontal diffusion in stratified vertical shear flow. Tellus **24**: 17–28. doi:10.1111/j.2153-3490.1972.tb01529.x

Kundu, P., I. Cohen, and D. Dowling. 2012. Fluid mechanics, 920 pp. Academic Press.

Large, W. G., J. C. McWilliams, and S. C. Doney. 1994. Oceanic vertical mixing: A review and a model with a nonlocal boundary layer parameterization. Rev. Geophys. **32**: 363–403. doi:10.1029/94RG01872

Lawrence, G. A., N. Yonemitsu, and J. Ellis. 1995. Natural dispersion in a small lake. Limnol. Oceanogr. **40**: 1519–1526. doi:10.4319/lo.1995.40.8.1519

MacKinnon, J. A., and M. C. Gregg. 2005. Near-inertial waves on the New England shelf: The role of evolving stratification, turbulent dissipation, and bottom drag. J. Phys. Oceanogr. **35**: 2408–2424. doi:10.1175/JPO2822.1

Mortimer, C. H. 2004. Lake Michigan in motion: Responses of an inland sea to weather, earth-spin, and human activities. Univ. of Wisconsin Press.

Murthy, C. 1976. Horizontal diffusion characteristics in Lake Ontario. J. Phys. Oceanogr. **6**: 76–84. doi:10.1175/1520-0485(1976)006<0076:HDCILO>2.0.CO;2

North, E. W., Z. Schlag, R. R. Hood, M. Li, L. Zhong, T. Gross, and V. S. Kennedy. 2008. Vertical swimming behavior influences the dispersal of simulated oyster larvae in a coupled particle-tracking and hydrodynamic model of Chesapeake Bay. Mar. Ecol. Prog. Ser. **359**: 99–115. doi:10.3354/meps07317

Okubo, A. 1971. Oceanic diffusion diagrams. Deep-Sea Res. Oceanogr. Abstr. **18**: 789–802. doi:10.1016/0011-7471(71)90046-5

Peeters, F., A. Wüest, G. Piepke, and D. M. Imboden. 1996. Horizontal mixing in lakes. J. Geophys. Res. Oceans **101**: 18361–18375. doi:10.1029/96JC01145

Ross, O. N., and J. Sharples. 2004. Recipe for 1-D Lagrangian particle tracking models in space-varying diffusivity. Limnol. Oceanogr.: Methods **2**: 289–302. doi:10.4319/lom.2004.2.289

Saffman, P. G. 1962. The effect of wind shear on horizontal spread from an instantaneous ground source. Q. J. R. Meteorol. Soc. **88**: 382–393. doi:10.1002/qj.49708837803

Smith, R. 1982. Dispersion of tracers in the deep ocean. J. Fluid Mech. **123**: 131–142. doi:10.1017/S0022112082002985

Steinbuck, J. V., J. R. Koseff, A. Genin, M. T. Stacey, and S. G. Monismith. 2011. Horizontal dispersion of ocean tracers in internal wave shear. J. Geophys. Res. Oceans **116**: C11031. doi:10.1029/2011JC007213

Stocker, R., and J. Imberger. 2003. Horizontal transport and dispersion in the surface layer of a medium-sized lake. Limnol. Oceanogr. **48**: 971–982. doi:10.4319/lo.2003.48.3.0971

Sundermeyer, M. A., and J. R. Ledwell. 2001. Lateral dispersion over the continental shelf: Analysis of dye release experiments. J. Geophys. Res. Oceans **106**: 9603–9621. doi:10.1029/2000JC900138

Taylor, G. 1953. Dispersion of soluble matter in solvent flowing slowly through a tube. Proc. R. Soc. Lond. Ser. Math. Phys. Sci. **219**: 186–203. doi:10.1098/rspa.1953.0139

Taylor, G. 1954. The dispersion of matter in turbulent flow through a pipe. Proc. R. Soc. Lond. Ser. Math. Phys. Sci. **223**: 446–468. doi:10.1098/rspa.1954.0130

Thupaki, P., M. S. Phanikumar, D. J. Schwab, M. B. Nevers, and R. L. Whitman. 2013. Evaluating the role of sediment-bacteria interactions on *Escherichia coli* concentrations at beaches in southern Lake Michigan. J. Geophys. Res. Oceans **118**: 7049–7065. doi:10.1002/2013JC008919

Van der Lee, E. M., and L. Umlauf. 2011. Internal wave mixing in the Baltic Sea: Near-inertial waves in the absence of tides. J. Geophys. Res. Oceans **116**: 1–16. doi:10.1029/2011JC007072

Visser, A. 1997. Using random walk models to simulate the vertical distribution of particles in a turbulent water column. Mar. Ecol. Prog. Ser. **158**: 275–281. doi:10.1016/j.jmarsys.2005.08.003

Wells, M. G., S. A. Bailey, and B. Ruddick. 2011. The dilution and dispersion of ballast water discharged into Goderich Harbor. Mar. Pollut. Bull. **62**: 1288–1296. doi:10.1016/j.marpolbul.2011.03.005

Wüest, A., A. Lorke, and G. Likens. 2009. Small-scale turbulence and mixing: Energy fluxes in stratified lakes. Encycl. Inland Waters **1**: 628–635. doi:10.1016/B978-012370626-3.00084-3

Wynne, T. T., R. P. Stumpf, M. C. Tomlinson, D. J. Schwab, G. Y. Watabayashi, and J. D. Christensen. 2011. Estimating cyanobacterial bloom transport by coupling remotely sensed imagery and a hydrodynamic model. Ecol. Appl. **21**: 2709–2721. doi:10.1890/10-1454.1

Zedler, S. E., T. D. Dickey, S. C. Doney, J. F. Price, X. Yu, and G. L. Mellor. 2002. Analyses and simulations of the upper ocean's response to Hurricane Felix at the Bermuda Testbed Mooring site: 13–23 August 1995. J. Geophys. Res. **107**: 25-1–25-29. doi:10.1029/2001JC000969

Acknowledgments

This work was supported by NSF grant OCE-1030842 (Physical Oceanography Division). This is GLERL contribution #1774.

Submitted 23 February 2015
Revised 2 July 2015
Accepted 13 August 2015

Associate editor: Craig Stevens